JOURNAL OF OPTOELECTRONICS AND ADVANCED MATERIALS Vol. 9, No. 1, January 2007, p. 30 - 36

Invited Lecture

Vibrational spectroscopy methods in the characterization of nanostructured materials

M. J. ŠĆEPANOVIĆ*, M. GRUJIĆ-BROJČIN, Z. DOHČEVIĆ-MITROVIĆ, Z. V. POPOVIĆ
Center for Solid State Physics and New Materials, Institute of Physics, 11080 Belgrade, Pregrevica 118, Serbia

The use of the vibrational spectroscopy techniques (Raman and infrared) in the characterization of nanostructured materials is presented. The Raman spectroscopy method has been used for structural characterization of nanomaterials. The estimation of average grain size and size distribution, layer thickness, strain effects, presence of defects and nonstoichiometry by Raman spectroscopy is illustrated in the case of CeO_2, TiO_2, and ZnO nanopowders, as well as nanostructured ZnSe/SiO_x multilayers. The infrared spectroscopy method has been applied on TiO_2 and ZnO nanopowders and SiO_x thin films in the analysis of grain size and shape, porosity, the nature of the surface bonds and reactions at the nanoparticle surface.

(Received November 1, 2006; accepted December 21, 2006)

Keywords: Nanomaterials, Raman spectroscopy, Infrared spectroscopy

1. Introduction

Raman spectroscopy is a powerful tool for the characterization of nano-sized materials and structures. It is widely used for the study of phonon confinement effects, the effect of the increase in local temperature, strain and substitutional effects, lattice distortion, the presence of structural defects and nonstoichiometry in different kinds of nanomaterial. Recent progress in the use of Raman spectroscopy for nanomaterials characterization is summarized in Ref. [1].

Several factors like phonon confinement [2-8], strain [6, 9], non–homogeneity of the size distribution [6, 10], defects and nonstoichiometry [6, 11], as well as anharmonic effects due to temperature increases [12] can contribute to the changes in the peak position, linewidth and shape of the Raman modes in nanostructures. The factors which play an important role in Raman spectra depend on the structural characteristics of nanomaterials, the first of which is the dimensionality of the nanostructure [8, 13]. The grain size and its distribution, the existence of mixed phases, the value and type of the strain (compressive or tensile), deviations from stoichiometry as well as type of stoichiometric defects, etc. also have great influence on the Raman spectra of nanomaterials. We shall demonstrate here how the Raman spectroscopy method can be used for the characterization of nano-powdered oxides like TiO_2, CeO_2 and ZnO, as well as nanostructured ZnSe/SiO_x multilayers.

The shift, broadening and asymmetric shape of the Raman modes, observed in these nanomaterials, are compared to spectra obtained from the phenomenological model, which takes into account disorder effects through the breakdown of the k=0 Raman-scattering selection rule, as well as the anharmonicity, which is incorporated through the 3- and 4-phonon decay processes. The application of a three-dimensional (3D) confinement model appropriate to isolated or loosely connected nanoparticles shows that the shift and broadening of the Raman peak in some nanopowders are dominated by the strong confinement and inhomogeneous strain (CeO_2), while in the others anharmonic effects (TiO_2) or tensile strain (ZnO) plays the main role. On the other hand, the shift and asymmetric broadening of the Raman mode in nanostructured ZnSe/SiO_x multilayers is analyzed by a one-dimensional (1D) confinement model, appropriate for very thin films or quantum wells. Due to the low dimensionality of these structures, the surface phonon modes are also observed.

The infrared (IR) spectra of nanocrystalline solids differ from the spectra of monocrystals, due to the polycrystalline character and island structure of nanoparticles. From IR spectra, it is possible to get information about the energy gap, grain size, porosity, nature of the surface bonds, and chemical reactions occurring at the nanoparticle surface.

Applying the effective medium theories [14] to interpret the infrared reflectivity spectra of TiO_2 nanopowders, we established the relation between the spectra shapes and porosity of nanopowders. Differences between the IR reflection spectra of mechanically activated and commercial ZnO powders pointed to the changes in the powder microstructure, as well as the presence of unintentionally introduced impurities during the activation. The IR absorbance spectra of rapidly annealed SiO_x thin films with different oxygen content were analyzed, in order to make qualitative estimations of the annealing effects on the SiO_x film structure and stability. It was shown that the IR spectra undergo drastic changes at longer annealing times, indicating a reduction in the oxygen content and an increase in the film porosity.

2. Raman spectroscopy

2.1. Phenomenological phonon confinement model

The phonons in nanocrystals are confined in space and all phonons over the entire Brillouin zone will contribute to the first-order Raman spectra. The weight of the off-center phonons increases as the crystal size decreases and the phonon dispersion causes an asymmetric broadening and a shift of the Raman mode. According to the phenomenological work of Richter et al. [7] and Campbell et al. [8] for a spherical particle of diameter L and a Gaussian confinement function, the resulting Raman intensity $I(\omega)$ can be presented as a superposition of weighted Lorentzian contributions over the whole Brillouin zone:

$$I(\omega)=\sum_{1}^{m}\int_{0}^{\infty}\rho(L)\times \times\int_{BZ}\frac{\exp\left(\frac{-q^2L^2}{8\beta}\right)d^3q}{\left\{\omega-\left[\omega_i(q,T)+\Delta\omega_i(q,L)\right]\right\}^2+\left(\frac{\Gamma(T)}{2}\right)^2}\cdot dL \quad (1)$$

where $\rho(L)$ is the particle size distribution, q is the wave vector expressed in units of π divided by the value of the unit cell parameter, and $\Gamma(T)$ is the mode line width at temperature T. The sum is carried over m dispersion curves $\omega_i(q, T)$, depending on mode degeneration. The factor β varies from β =1 in the Richter confinement model [7] to β =$2\pi^2$ in the Campbell model [8], depending on the confinement boundary conditions in different nanomaterials. The properties of the Raman mode simulated by this model strongly depend on the mean particle size and unit cell parameter, as well as the choice of the values of $\Gamma(T)$, and β. Also, the particle size distribution $\rho(L)$ and the shape of the phonon dispersion relations $\omega_i(q)$ has a great influence on the position and asymmetry of the calculated spectra. Sometimes, different combinations of these choices can give similar results. For instance, the application of a strong confinement condition, i.e. a large confinement parameter β in combination with a phonon dispersion curve with a small slope [4, 15], can give similar calculated results for Raman modes in nanocrystals as does a weaker β and dispersion with a greater slope [2, 12].

A lattice constant variation with decreasing particle size, due to the microstrain effects, is found in various nanocrystalline materials [16, 17]. The lattice parameter change is incorporated in model and the strain is considered to be uniform within each particle. This average strain produces changes in the lattice parameter and affects the Raman peak position. The Raman mode centered at T_i shifts by $\Delta\omega(q,L)=-3\gamma_i(q)T_i(q)\times(\Delta a/a_0)$, where γ_i is a mode Grüneisen parameter and Δa is the measured change of the lattice parameter relative to the bulk value a_0. The sign of the lattice constant variation Δa indicates tensile (positive) or compressive (negative) strain.

The three-dimensional (3D) phonon confinement model is appropriate for powders, quantum dots, etc. where the infinitesimal volume element in the integral (Eq. (1)) can be written as $d^3q \propto q^2dq$. For 2D confinement (quantum wires, etc.) it is $d^3q \propto qdq$ and for 1D (quantum wells, etc.) $d^3q \propto dq$.

Anharmonic effects, due to temperature increases [12], also contribute to the changes in the peak position and linewidth of the Raman mode. Anharmonicity is incorporated through the 3- and 4-phonon decay channels in the scattering process [9, 18]:

$$\omega(q,T)=\omega_0(q)+\Delta(T) \quad (2)$$

$$\Delta(T)=A_1\left[1+\sum_{j=1}^{2}\frac{1}{\exp(x_j)-1}\right]+ +A_2\left[1+\sum_{k=1}^{3}\frac{1}{\exp(y_k)-1}+\frac{1}{(\exp(y_k)-1)^2}\right] \quad (3)$$

$$\Gamma(T)=\Gamma_0+\Delta\Gamma(T) \quad (4)$$

$$\Delta\Gamma(T)=B_1\left[1+\sum_{j=1}^{2}\frac{1}{\exp(x_j)-1}\right]+ +B_2\left[1+\sum_{k=1}^{3}\frac{1}{\exp(y_k)-1}+\frac{1}{(\exp(y_k)-1)^2}\right] \quad (5)$$

The first terms in Eq. (3) and (5) describe the coupling of the optical phonon to two lower-energy phonons (3-phonon coupling, with $x_1=x_2=\hbar\omega_0/2kT$) which is proportional to T at higher temperatures, and the second terms describe the coupling to three phonons (4-phonon coupling, with $y_1=y_2=\hbar\omega_0/3kT$) which is proportional to T^2 at higher temperatures.

2.2. Experimental results

2.2.1. CeO_2 nanopowder

The fluorite structure CeO_2 has a Raman active triply degenerate F_{2g} mode at 465 cm^{-1} [19]. In nanosized $CeO_{2-\delta}$ samples, this mode is centered at 454 cm^{-1}, showing a stronger redshift than that reported by other authors for nano CeO_2 samples [20, 21]. It is also slightly asymmetric, with increased linewidth, relative to the bulk counterpart (the inset in Fig. 1)

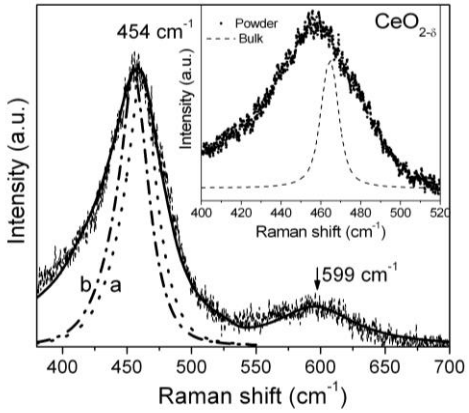

Fig. 1. First–order Raman spectrum of $CeO_{2-\delta}$ nanopowder (dashed line) and fitted spectrum (full line) using the combined effect of inhomogeneous strain and confinement together with simulated spectra based on Campbell's (a) and Spanier's model for the averaged strain (b). The peak at 599 cm^{-1} is associated with intrinsic oxygen vacancies in ceria nanopowders. Inset: Raman spectra of $CeO_{2-\delta}$ nanopowder and a bulk sample, showing size-dependent changes in the peak position and line shape.

To obtain the best fit to the Raman spectrum of $CeO_{2-\delta}$ nanopowder, we used the model presented by Eq. (1), incorporating both phonon confinement and the inhomogeneous strain effect [22]. The natural full width of the F_{2g} mode is Γ_0= 10 cm^{-1} [19], while the average particle diameter is taken to be L_0 = 7 nm. The phonon dispersion of the F_{2g} mode, $T_i(q)$, is represented by parabolic fits to the Nakajima dispersion curves for CeO_2 [23]. To simulate the shift and linewidth of the F_{2g} mode in $CeO_{2-\delta}$ nanopowders, a higher degree of phonon confinement than that in Spanier's model [9] was applied, i.e. $\beta \sim 4\pi^2$.

A Gaussian particle size distribution with fixed parameters Γ_0 and L_0 was used in the fitting procedure, while the variable parameter was the Gaussian width (w) related to the standard deviation as $\sigma = 0.693w$. The variation of the lattice constant Δa versus crystal size L is $\sim (k/L^2)$ [9, 20] where k =0.0939 nm^3, a_0=0.54087 nm and γ_i =1.24 [19]. The calculated Raman spectrum (solid line), using the model with confinement $\beta \sim 4\pi^2$ and inhomogeneous strain effects for pure ceria nanopowder, together with experimental data (dotted line), are presented in Fig. 1.

The simulated Raman spectra based on Campbell's and Spanier's models for the averaged strain are also presented in Fig. 1, for comparison. The particle size evaluated from this model is in good agreement with the X-ray diffraction (XRD) results. The strain shift to lower energies of the F2g mode and its asymmetric broadening can be very well explained by an inhomogeneous strain effect associated with the dispersion in particle size using the phonon confinement model with a stronger boundary condition than those previously reported for CeO_2 nanopowders.

2.2.2. TiO_2 nanopowder

Raman spectra of laser synthesized [24] anatase TiO_2 nanopowder and calculated spectra at several temperatures (25, 300 and 555 K) are shown in Fig. 2.

In the calculation of the Raman intensity of the lowest frequency E_g mode at ~144 cm^{-1}, we used the phonon confinement model (Eq. (1)) combined with a temperature dependent linewidth $\Gamma(T)$ and phonon dispersion $\omega_i(q, T)$ due to anharmonic effects (Eqs. (2-5)). The average crystallite size was L_0=12.5 nm, according to XRD measurements. The confinement factor $\beta \approx 16$ was used. From scanning electron microscopy (SEM) results, we assumed an asymmetric Gaussian particle size distribution with an asymmetry factor A=0.41. The strain value obtained from XRD was relatively small (σ =0.02 %), therefore its influence on the Eg mode was neglected. Although nonstoichiometry due to laser irradiation in vacuum can cause a considerable blueshift and broadening of the E_g mode [2, 6, 11], these effects are relatively small in our sample (~1 cm^{-1}). It seems that the presence of nonstoichiometric defects in this sample preferably induces the appearance of a new mode at ~137 cm^{-1} at room temperature, which can be related to the presence of a small number of nanoparticles of titanium [25].

The main problem when using this model is the lack of experimental dispersion relations of anatase TiO_2 from inelastic neutron scattering, and the only dispersions have been computed by Mikami et al. [26]. In this paper, the dispersion relations for anatase are approximately expressed, according to these theoretical curves, in the cosine form [12]:

$$\omega_i(q,T) = \omega_0(T) + B_i\left(1-\cos(q\pi)\right) \tag{6}$$

where $\omega_0(T)$ is the frequency of the E_g mode in Γ point at temperature T, while the B_i values are calculated to match the phonon dispersion curves.

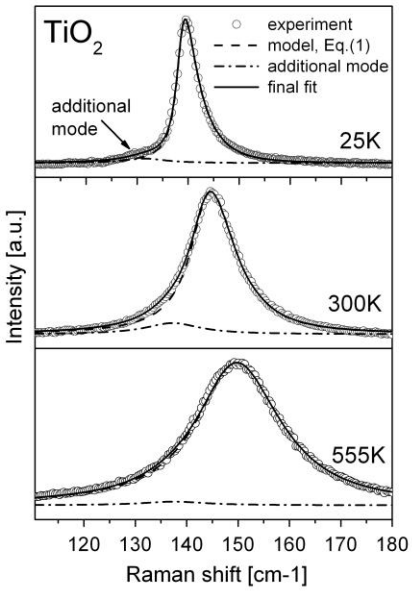

Fig. 2. The experimental (open circles) and calculated (solid lines) spectra of anatase TiO_2 nanopowder.

The values of $\omega_0(T)$ and $\Gamma(T)$ at a specified temperature were treated as adjustable parameters in the fitting procedure, and the obtained temperature dependence of these parameters was in accordance with the anharmonic behavior defined by Eqs. (2-5).

In the Figs. 3a and 3b, the calculated contributions of confinement and anharmonic effects to the shift and linewidth of the Raman E_g mode at different temperatures are presented separately. As expected, these contributions are comparable at low temperatures, while the ones due to anharmonic effects at high temperatures far exceed the contribution of the confinement effect. Neglecting the influence of the anharmonic effect on the E_g Raman mode, even at room temperature, leads to great inaccuracy in the application of the phonon confinement model and determination of corresponding parameters in the case of TiO_2 nanopowders.

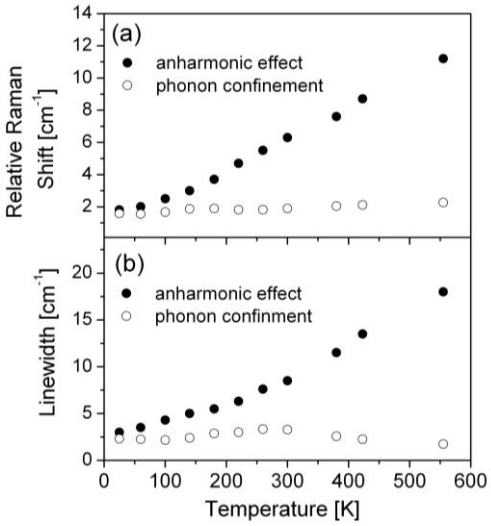

Fig. 3. The experimental dependence of the E_g peak position (a) and linewidth (b) on the measured (open circles) and calculated (closed circles) temperature in comparison with corresponding data calculated by the anharmonic relations (solid lines).

2.2.3. ZnO powders

Raman spectra of commercial zinc oxide powder (ZnO(0)) and mechanically activated powders, with a grinding time of 30 min, (ZnO(30)) and 300 min (ZnO(300)) are presented in Fig. 4.

The Raman modes of the original sample can be assigned to the Raman spectra of the bulk ZnO [27]. In the spectra of activated ZnO powders, the intensity of all observed modes decreases and their linewidth increases, while the E_2^{high} and E_1(LO) modes shift to lower wave numbers with increasing activation time.

As the grain size in the powders is relatively large (44 nm for ZnO(300), 106 nm for ZnO(30) and 190 nm for ZnO(0)), the application of the phonon confinement model according to Eq. (1) gives a symmetrical Raman mode shape without a shift. Having in mind the microstrain values (from XRD), which drastically increase with activation time (~0.04 % for ZnO(0), ~0.32 % for ZnO(30), and ~0.78 % for ZnO(300)) [28], the broadening and redshift of the E_2^{high} and E_1(LO) modes originate from tensile strain effects introduced by mechanical activation, rather then from the effects of phonon confinement.

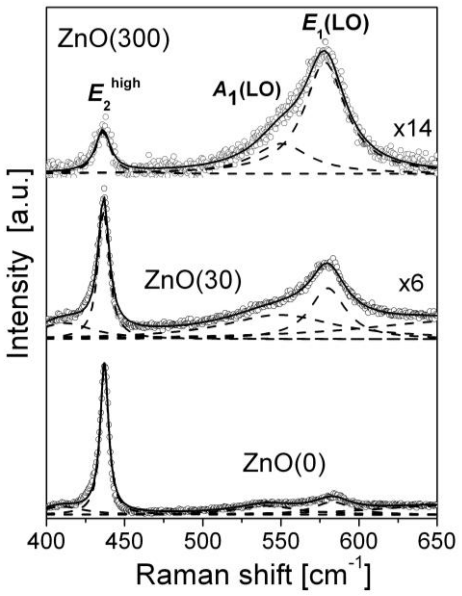

Fig. 4. Experimental (o) *and calculated (thick line) Raman spectra of ZnO powder. The thin lines denote Lorentzian peaks originating from the assigned Raman modes.*

2.2.4. ZnSe/SiO_x multilayers

The experimental and calculated Raman spectra of ZnSe/SiO_x multilayers with ZnSe layer thicknesses of 2.0, 3.5, 7.0 and 10 nm [29] are shown in Fig. 5. The calculated spectra were obtained as the sum of contributions of longitudinal (LO) and transverse (TO) optical modes and the surface phonon mode (SP).

The influence of the ZnSe layer thickness on the frequency shift and asymmetrical broadening of the LO Raman mode at ~251 cm^{-1} is analyzed by applying a one-dimensional (1D) phonon confinement model, where $d^3q \propto dq$ is assumed in Eq. (1).

The calculations were performed with the following parameters: intrinsic line width Γ_0 =12.5 cm^{-1}, confinement factor $\beta \approx 12$, and a Gaussian layer thickness distribution with halfwidth $0.10L_0$.

With decreasing layer thickness, the Raman mode position is blueshifted and broadened, and an asymmetric lineshape is present, especially in samples with layer thicknesses of 2 and 3.5nm.

Applying the 1D phonon confinement model gives very good results in the estimation of the LO mode position and width, and allows us to assume that ZnSe in ZnSe/SiO_x multilayers can be treated as nanolayers rather than isolated or loosely connected nanoparticles.

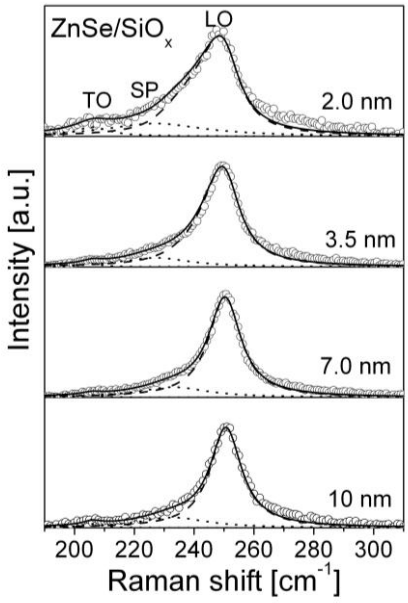

Fig. 5. Normalized experimental Raman spectra (o) of $ZnSe/SiO_x$ multilayers and calculated results (thick line). The dotted lines denote TO and SP Lorentzian peaks. The dashed line represents the LO mode calculated fro the 1D phonon confinement model.

3. Infrared spectra

3.1. TiO_2 nanopowders

The IR reflection spectra of TiO_2 nanopowder samples with different particle sizes: 14 nm, 16 nm and 23 nm are shown in Fig.6. The calculations of IR spectra were done using the Bruggeman effective medium approximation (EMA), which takes into account the macroscopic volume fractions and local microstructural geometry of the material [14, 30].

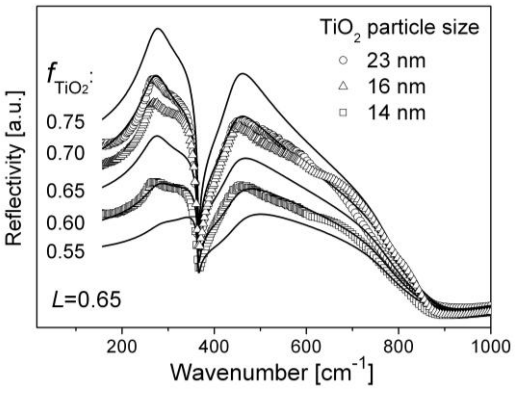

Fig. 6. Experimental IR spectra of TiO_2 nanopowders with the particle size denoted. Calculated IR spectra (—) of the samples obtained by generalized Bruggeman EMA for different volume fractions f_{TiO2} and pore shape factors $L=0.65$.

The IR spectrum of anatase TiO_2 nanopowders was analyzed in three steps, using (i) bulk data, (ii) the polycrystalline character of the nanopowder and (iii) the porosity of the nanopowder, together with the influence of the pore shape [31]. The polycrystalline character of the nanopowder was introduced by determining the dielectric function $\varepsilon_{pc}(\omega)$ from

$$\frac{1}{3}\left(\frac{\varepsilon_{||}-\varepsilon_{pc}}{\varepsilon_{||}+2\varepsilon_{pc}}\right)+\frac{2}{3}\left(\frac{\varepsilon_{\perp}-\varepsilon_{pc}}{\varepsilon_{\perp}+2\varepsilon_{pc}}\right)=0 \qquad (7)$$

where $\varepsilon_{||}(\omega)$ and $\varepsilon_{\perp}(\omega)$ are the dielectric functions of single crystal anatase TiO_2 in two different polarizations with respect to the c axis ($E \parallel c$ and $E \perp c$). Eq. (7) was deduced from the Bruggeman EMA [30]. It assumes the pellet to be a nanocomposite of two fictitious isotropic materials, having dielectric functions $\varepsilon_{||}(\omega)$ and $\varepsilon_{\perp}(\omega)$, with volume fractions 1/3 and 2/3, respectively. Both functions are determined from the shape of the reflectivity spectra of the anatase TiO_2 single crystal, using a factorized form of the dielectric function,

$$\varepsilon(\omega)=\varepsilon_{\infty}\prod_{n}\frac{\omega_{LOn}^2-\omega^2+i\omega\gamma_{LOn}}{\omega_{TOn}^2-\omega^2+i\omega\gamma_{TOn}} \qquad (8)$$

with TO and LO frequencies (ω_{TO} and ω_{LO}), as well as corresponding damping factors (γ_{TO}, γ_{LO}). These parameters are listed in Table 1 of Ref. [32].

As nanophase TiO_2 is a porous material with a relatively large specific surface, the porosity of the nanopowder was included in modeling its dielectric function. The best agreement between the calculated and experimental results was obtained by the generalized Bruggeman EMA [30], which introduces the effect of pore shape by using the adjustable depolarization factor L for ellipsoidal voids ($L = 1/3$ for spherical cavities and $1/3 < L < 1$ for prolate spheroidal cavities):

$$\left(\frac{\varepsilon_A-\varepsilon_{effg}}{\varepsilon_{effg}+L_j(\varepsilon_A-\varepsilon_{effg})}\right)f_A = \left(\frac{\varepsilon_B-\varepsilon_{effg}}{\varepsilon_{effg}+L_j(\varepsilon_B-\varepsilon_{effg})}\right)f_B=0 \qquad (9)$$

The porous nanopowder with the dielectric function ε_{eff} is assumed to be a nanocomposite of polycrystalline TiO_2 (with dielectric function ε_{pc} from Eq. (7)) and air ($\varepsilon_{\infty} = 1$), with volume fractions f_{TiO2} and f_{air}, respectively. Note that $f_{air} = 1 - f_{TiO2}$, expressed in percentage terms, corresponds to the macroscopic value of the nanopowder porosity. Generally, a decrease in the TiO_2 volume fraction results in a decrease in the IR reflectivity, due to the greater air fraction in the powder.

In Fig. 6. the calculated spectra for the L=0.65 and f_{TiO2} from 0.55 to 0.75 are presented. It is obvious that a decrease in f_{TiO2} also causes a broadening of IR features. The physical reason for such behavior lies in the fact that the smaller the value of f_{TiO2}, i.e. the greater the porosity, the smaller is the particle size.

Good qualitative and quantitative agreement between the theoretical and experimental spectra and also compatibility of the fitting results with the physical properties of TiO_2 nanopowders, confirm the validity of the proposed model [32].

3.2. ZnO powders

The far infrared (IR) reflectivity spectra of ZnO commercial and mechanically activated powders (as mentioned in section 2.2.3) are shown in Fig. 7.

The differences between the IR spectra of the original and activated samples point to changes in the powder microstructure. Moreover, a new IR band at ~380 cm^{-1} appears in the spectrum of ZnO(300), besides the A_1 and E_1 infrared active modes characteristic of ZnO, indicating the presence of a small amount of iron-oxides due to long time grinding in a vibro-mill with steel rings.

This study confirms IR spectroscopy methods as very useful in the determination of the microstructural properties and detection of unintentionally introduced impurities in the material.

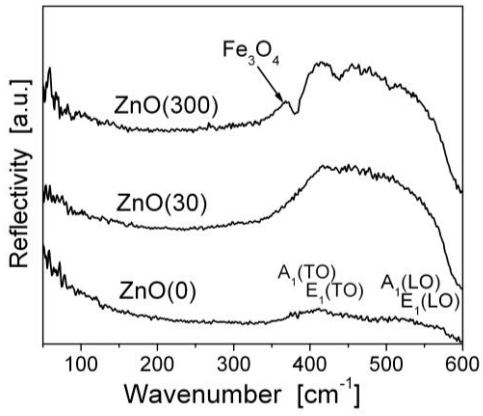

Fig. 7. IR reflectivity spectra of commercial (ZnO(0)) and mechanically activated ZnO powders for 30 (ZnO(30)) and 300 (ZnO(300)) minutes.

3.2. SiO_x thin films

The infrared (IR) absorbance spectra of SiO_x films with $1.15 \leq x \leq 1.7$, rapidly thermally annealed at 1100°C in vacuum for 15 and 30 s, are shown in Fig. 8 [33]. A great number of modes is present in the IR spectra, pointing to the amorphous nature of SiO_x films. The positions and shape of the IR modes from SiO_x thin amorphous films substantially differ from those of the bulk counterpart. Local defects and nearest-neighbor bonding associated with Si-O bonds in a tetrahedral arrangement all generate features in the IR spectra.

The frequency of the TO stretching mode decreases from 1039 (x=1.15) to 1012 cm^{-1} (x=1.4), then slowly rises with x, reaching 1022 cm^{-1} for the SiO_x sample with x=1.7. The frequency of the strongest mode in SiO_x films annealed for 30 s in vacuum is lower than for films annealed for 15 s. That can be explained by assuming a decrease in oxygen content and a parallel increase in the layer porosity, as a result of oxygen loss after a longer annealing time.

In the SiO_x films, two shoulders are visible at the high-energy side of the most pronounced absorption band. The frequency of the greater one is about 1170 (1156) cm^{-1} in films annealed for 15 (30) s. This band is referred to the LO-stretching mode of SiO_x films [29, 34], which is located at ~1280 cm^{-1} in SiO_2. A decrease in the frequency of this mode in SiO_x films after annealing for 30 s in vacuum implies a weakening of the stretching mode. After annealing of 30 s, its intensity is lower then after 15 s annealing, which is additional proof that loss of the oxygen has happened. One can conclude that both the intensity and frequency of this mode increase with increasing oxygen content, and with decreasing pore volume fraction.

A new IR feature appears at 1106 cm^{-1} in all spectra, as a small shoulder at the high energy side of the TO stretching mode. It is hardly distinguished in films annealed for 15 s and seems to stay unchanged. In films annealed for 30 s, this mode becomes easily visible, and it can be attributed to interstitial oxygen in the c-Si substrate [33, 35].

In this study, it has been shown that IR spectra undergo drastic changes at longer annealing times, indicating a decrease in the oxygen content and an increase in the film porosity in films annealed for 30 s when compared with those annealed for 15 s.

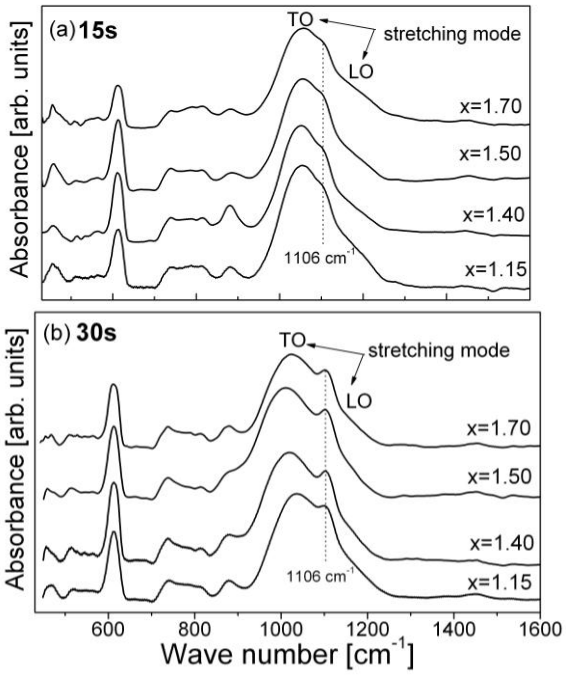

Fig. 8. Infrared absorbance spectra of SiO_x films recorded at room temperature in the spectral range 430 to 1600 cm^{-1}: a) films annealed for 15 s, b) films annealed for 30 s. All spectra correspond to the same scale.

4. Conclusions

We have shown that Raman and infrared spectroscopy are very effective and nondestructive optical techniques for the characterization of nanostructure materials.

The experimental Raman spectra presented here, as well as their analyses based on a phonon confinement model, confirm Raman spectroscopy as a powerful technique for determining the structural properties of nanomaterials. From these measurements, we can estimate the average particle size (layer thickness) and its distribution, strain and anharmonic effects, nonstoichiometry and structural defects.

The infrared spectra give the possibility to obtain a wide range of information on nanostructured materials, such as the particle size, porosity, structural defects, nonstoichiometry, and the nature of the surface bonds, as well as the chemical reactions occurring at the nanoparticle surface.

Acknowledgement

This work was supported by the Serbian MSEP under the project No.141047.

References

[1] G. Gouadec, P. Colomban, Progress in Crystal Growth and Characterization of Materials (2006) in press.
[2] A. Li Bassi, D. Cattaneo, V. Russo, C. E. Bottani, E. Barborini, T. Mazza, P. Piseri, P. Milani, F. O. Emst, K. Wegner, S. E. Pratsinis, J. Appl. Phys. **98**, 074305 (2005).
[3] S. Kelly, F. H. Pollak, and M. Tomkiewicz, J. Phys. Chem. B **101**, 2730 (1997).
[4] D. Bersani, P. P. Lottici, Appl. Phys. Lett. **72**, 73 (1998).
[5] W. F. Zhang, Y. L. He, M. S. Zhang, Z. Yin, Q. Chen, J. Phys. D: Appl. Phys. **33**, 912 (2000**).**
[6] M. J. Šćepanović, M. U. Grujić-Brojčin, Z. D. Dohčević-Mitrović, Z. V. Popović, Materials Science Forum **518**, 101 (2006).
[7] H. Richter, Z.P. Wang, L. Ley, Solid State Commun. **39**, 625 (1981).
[8] I. H. Campbell, P. M. Fauchet, Solid State Commun. **58**, 739 (1984).
[9] J. E. Spanier, R. D. Robinson, F. Zhang, S. W. Chan, I. P. Herman, Phys. Rev. B **64**, 245407 (2001).
[10] D. R. Santos, I. L. Torriani, Solid State Commun. **85**, 307 (1993).
[11] J. C. Parker, R. W. Siegel, Appl. Phys. Lett. **57**, 943 (1990).
[12] K. R. Zhu, M. S. Zhang, Q. Chen, Z. Yin, Phys. Lett. A **340**, 220 (2005).
[13] A. K. Arora, M. Rajalakshmi, T. T. Ravindran, in Encyclopedia of Nanoscience and Nanotechnology, ed. H. S. Nalwa, Vol. X, p.1 (2004).
[14] J. E. Spanier, I. P. Herman, Phys. Rev. B **61** 10437 (2000).
[15] M. Ivanda, S. Musić, M. Gotić, A. Turković, A. M. Tonejc, O. Gamulin, J. Mol. Struc. **480**, 641 (1999).
[16] S. H. Tolbert, A. P. Alvisiatos, Annu. Rev. Phys. Chem. **46**, 595 (1995).
[17] K. Lu, Y.H. Zhao, Nanostruct. Mater. **12**, 559 (1999).
[18] M. Balkanski, R. F. Wallis, E. Haro, Phys. Rev. B **28**, 1928 (1983).
[19] W. H. Weber, K. C. Hass, J. R. McBride, Phys. Rev. B **48**, 178 (1993).
[20] F. Zhang, S. W. Chan, J. E. Spanier, E. Apak, Q. Jin, R. D. Robinson, I. P. Herman, Appl. Phys. Lett. **80**, 127 (2002).
[21] M. D. Hernandez-Alonso, A. B. Hugria, A. Martinez-Arias, J. M. Coronado, J. C. Conesa, J. Soria, M. Fernandez-Garcia, Phys. Chem. Chem. Phys. **6**, 3524 (2004).
[22] Z. D. Dohčević-Mitrović, M. J. Šćepanović, M. U. Grujić-Brojčin, Z. V. Popović, S. B. Bošković, B. M. Matović, M. V. Zinkevich, F. Aldinger, Solid St. Commun. **137**, 387 (2006).
[23] A. Nakajima, A. Yoshihara, M. Ishigame, Phys. Rev. B **50**, 13297 (1994).
[24] F. Curcio, M. Musci, N. Notaro, C. Nannetti, Appl. Surf. Sci. **36**, 52 (1989).
[25] R. J. Nemanich, C. C. Tsai, G. A. N. Connell, Phys. Rev. Lett. **44**, 273 (1980).
[26] M. Mikami, S. Nakamura, O. Kitao, H. Arakawa, Phys. Rev. B **66**, 155213 (2002).
[27] C. A. Arguello, D. L. Rousseau, S. P. S. Porto, Phys. Rev. **181**, 1351 (1969).
[28] M. Šćepanović, T. Srećković, K. Vojisavljević, M. M. Ristić, Sci. Sintering **38,** 169 (2006).
[29] D. Nesheva, I. Bineva, Z. Levi, Z. Aneva, Ts. Merdzhanova, J. C. Pivin, Vacuum **68**, 24 (2003).
[30] D. A. G. Bruggeman, Ann. Phys. **24**, 636 (1935).
[31] F. Gervais, 1983 Infrared and Millimeter Waves vol 8, ed K J Button (New York: Academic)
[32] M. Grujić-Brojčin, M. J. Šćepanović, Z. D. Dohčević-Mitrović, I. Hinić, B. Matović, G. Stanišić, Z. V. Popović, J. Phys. D: Appl. Phys. **38**, 1415 (2005).
[33] A. Milutinović, Z. Dohčević-Mitrović, D. Nesheva, M. Šćepanović, M. Grujić-Brojčin, Z. V. Popović, Mat. Sci. Forum (to be published).
[34] A. Brunet-Bruneau, S. Fisson, G. Vuye, J. Rivory, J. Appl. Phys. **87**, 7303 (2000).
[35] I. W. Boyd, J. I. B. Wilson, J. Appl. Phys. **53**, 4166 (1982).

*Corresponding author: maja@phy.bg.ac.yu